

# Investigation of Field Structure and Electron Behavior in the Near-Field of Hall Thrusters

A. W. Smith\* and M.A. Cappelli†

*Mechanical Engineering Department, Thermosciences Division, Stanford University, Stanford, CA, 94305*

The formulation and preliminary results of a 3-D discrete electron transport simulation are presented. Assuming a magnetic and electric field distribution in the near-field of a Hall thruster, a leapfrog time-integrating method is utilized to track electrons launched from a simulated cathode to obtain statistics including estimates of the Hall parameter and anode/beam current ratios. It is shown that, disregarding collisions or instabilities in the near-field, the Hall parameter is on the order of two, and the anode/beam current is on the order of 0.1 to 0.2. The need for a complete mesh of potential data throughout the near-field is highlighted. Results obtained with similar multi-step methods including the Adam's Bashforth method and variations of the leapfrog method are also briefly mentioned.

## Nomenclature

$\vec{B}$	= magnetic field
$\underline{\underline{B}}$	= magnetic field matrix
$\vec{E}$	= electric field
$\underline{\underline{I}}$	= identity matrix
$m_e$	= electron mass
$q$	= fundamental charge of the electron
$r$	= gyration radius
$\vec{V}, \vec{x}$	= velocity
$\vec{V}^a, \vec{V}^b$	= virtual velocities
$\vec{V}_0$	= initial velocity
$\vec{V}, \vec{x}$	= acceleration
$\vec{x}$	= position
$\omega_{ce}$	= electron cyclotron frequency
$\Delta t$	= time step
$\Delta t_{max}$	= maximum time step

## I. Introduction

ONE of the remaining insufficiently explained phenomena involving Hall thrusters concerns the distribution of the electron current leaving the cathode of these devices. It has been established that the majority of the current, on the order of 90%, enters the plume and acts to neutralize it, while the remaining small fraction reaches the anode of the Hall thruster. However, the details of how electrons travel from the cathode to the anode and into the plume are unknown. The source of the bright conical beam which emanates from the center pole of Hall

\* Ph.D. Candidate, Mechanical Engineering, Stanford University, Stanford, CA, 94305, Student Member AIAA.

† Professor, Mechanical Engineering, Stanford University, Stanford, CA, 94305, Member AIAA.

thrusters also remains inadequately explained. Fully understanding these features requires a detailed examination of electron transport in the near-field region of Hall thrusters.

Frequently, researchers studying near-field behavior of Hall thrusters utilize computer simulations of particle behavior in this region. One of the more common techniques is a hybrid-PIC (Particle-In-Cell) model with the electrons considered as a fluid continuum and the ions and neutrals treated as macroparticles often containing  $10^5$  or more virtual ions or neutrals. At a given point in time, knowledge of the distribution of charge throughout the computational domain allows for a calculation of the electric potential and, hence, the electric field. Such simulations proceed self-consistently with the particle movement influenced by the electric potential which is itself governed by the particle distribution.

While, with a large number of particles present in a domain, the electric potential can be solved for self-consistently, if the electric potential is determined experimentally, then a relatively small number of charged particles may be treated assuming no interactions between particles. This approximation holds if, in general, the magnitude of the interaction force between simulated particles is overwhelmed by the local electric fields. This is the current approach of this research. Clearly then, of fundamental importance to the proper execution of a 3-D discrete electron transport simulation are 3-D meshes of electric and magnetic potential or electric and magnetic field strength and direction throughout the simulation domain.

Numerous researchers have studied aspects of the electric potential in the near-field of Hall thrusters experimentally<sup>1-8</sup>. In addition, numerical studies have been undertaken which can produce potential distributions from self-consistent calculations<sup>9-11</sup>. However, many of these results present electric potential data in limited regions such as the centerline of the thruster. In the cases with a numerically obtained extensive electric potential map, the potential data often remain unverified experimentally. The thruster considered in this research is the Stanford Hall thruster. The electric potential for this thruster is currently inspired by published numerical results<sup>12</sup> fit to experimental data taken with the Stanford Hall thruster<sup>13</sup>.

The magnetic field structure is assumed to be dominated by the externally applied field of the thruster. In this case, the results of simulations are utilized to generate the mesh of magnetic fields needed. We make use of FEMM (Finite Element Method Magnetics)<sup>14</sup>, a finite element magnetic solver in which we have built a model of the Stanford Hall thruster, to obtain the magnetic field distribution. At the moment, the magnetic field is assumed to be axisymmetric, as is the electric field.

Collisions and instabilities are not treated by the preliminary simulations. Electrons released from a hypothetical cathode are tracked until they exit the simulation domain which is currently 0.6m by 0.6m by 0.3m in x, y, and z centered on the thruster centerline with z oriented axially outward. Fig. 1 shows a top down view of the simulated thruster in the computational domain. The thruster is shaded with the channel darkened. Details concerning the thruster geometry follow in the next section. After leaving the domain, particle statistics are cataloged including exit location and velocity as well as time in the domain. The particles are tracked primarily using a leapfrog integrator following Birdsall and Langdon<sup>15</sup> for the equations of motion, but some cases with another multi-step method referred to as the Adam's Bashforth method<sup>16</sup> are also presented for comparison and discussion. Results concerning the effective Hall parameter and current ratio (fraction of cathode current passing into the thruster versus out to the beam) are presented.

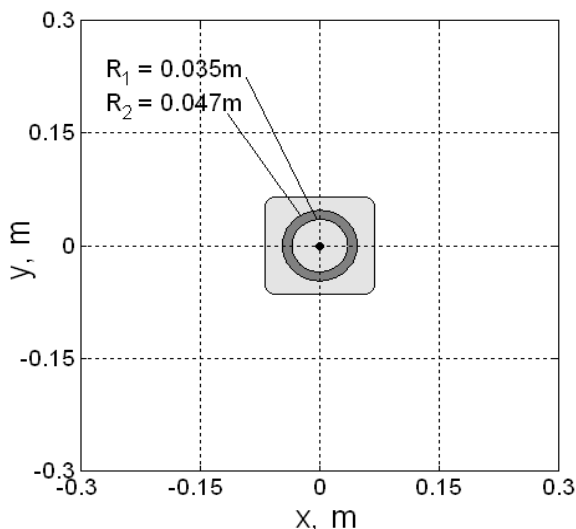


**Figure 1. Top view of simulation domain.**

## II. Near-Field Electric and Magnetic Field Structure

As previously mentioned, this research requires knowledge of the near-field electric potential and magnetic field structure. The electric potential is inspired by a potential surface generated via a hybrid-PIC simulation of an SPT-100 thruster<sup>12</sup>. Since the modeled thruster for the present 3D discrete electron simulations is the Stanford Hall thruster, the approximate potential derived from the SPT-100 numerical results was adjusted to fit potential

measurements for the Stanford Hall thruster<sup>13</sup>. The end result is currently an approximated potential which is not the direct result of simulations or measurements.

Fig. 2 is a mesh of the electric potential used for the subsequent calculations. At this point, the potential is

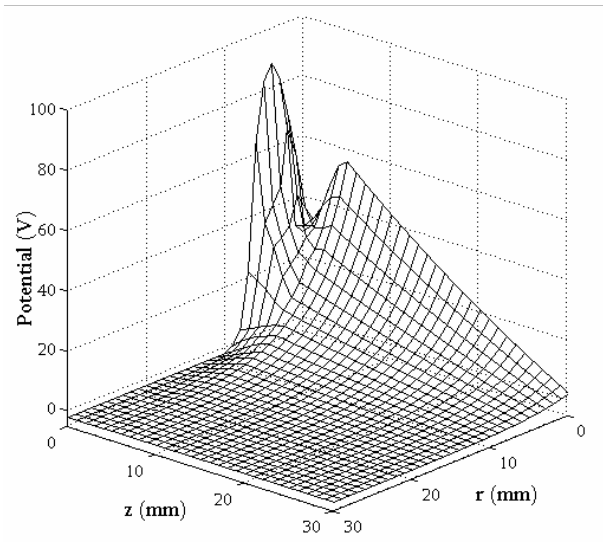


**Figure 2. Estimated electric potential surface for the stanford hall thruster.**

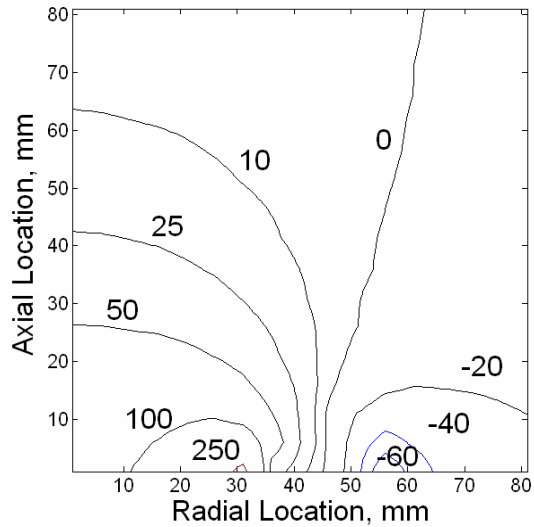


**Figure 3. Axial magnetic field strength for the Stanford hall thruster computed using FEMM**

assumed to be axisymmetric though this will be the topic of future research. The centerline of the thruster lies at  $r = 0$  in the figure so only half of the potential is shown. The data along the exit plane ( $r = 0$ ) and central axis ( $z = 0$ ) were fit to data previously measured for the Stanford Hall thruster while the body of the potential is an approximation. The potential reaches a maximum of 90V at the exit plane of the thruster at the center of the channel and quickly decays toward zero in the radial direction. Along the centerline of the thruster, the potential rises from near 25V at the exit plane to nearly 60V 5cm downstream before decaying with further distance in the axial direction. Important thruster dimensions to note when interpreting the figure include the channel width of 12mm with an inner radius of 35mm and an outer radius of 47mm which are also indicated in Fig. 1 above. The operating condition for which the experimentally measured potential applies was a discharge voltage of 250V. For detailed information regarding the dimensions of the Stanford Hall thruster, potential measurements, and operating conditions, see references<sup>13</sup>. For the simulations, the cathode point-source of electrons was placed 2cm axially out from the exit plane and 7cm radially outward. At this location, the estimated potential is 20V.

The magnetic field structure was determined using a modeled Stanford Hall thruster in FEMM. Fig. 3 shows the resulting axial magnetic field component generated using this software. The axial magnetic field strength is constant on a given contour in Fig. 3, and the bold values indicate the magnetic field strength in units of Gauss (G). FEMM is utilized to extract both the radial and axial components of the magnetic field, however, only the axial component is currently shown for conciseness. The maximum axial magnetic field strength at the exit plane of the thruster is 285G, and the absolute minimum is just less than -80G. The magnetic field strength quickly drops off from its maximum near-field value above 250G near the exit plane to less than 50G in magnitude within 3cm axially. The total magnetic field strength across the channel does not exceed 130G.

### III. Equations of Motion and Numerical Methods

#### A. Governing Equation of Motion

For the purposes of a particle treatment of electrons in fields which are assumed to be externally applied, the only equation of motion is Newton's Second Law with the particle acceleration occurring due to the Lorentz Force:

$$\vec{\ddot{x}} = \frac{q}{m_e} (\vec{E} + \vec{\dot{x}} \times \vec{B}) \quad (1)$$

where  $\vec{E}$  is the electric field,  $\vec{B}$  is the magnetic field,  $\vec{\ddot{x}}$  is the electron acceleration,  $\vec{\dot{x}}$  is the electron velocity,  $m_e$  is the electron mass, and  $q$  is the fundamental charge of the electron. This can be broken down into two first-order ordinary differential equations to facilitate numerical solution as:

$$\vec{\dot{V}} = \frac{q}{m_e} (\vec{E} + \vec{V} \times \vec{B}) \quad (2)$$

$$\vec{\dot{x}} = \vec{V} \quad (3)$$

where  $\vec{V}$  is the electron velocity.

## B. Numerical Integration of Governing Equations

Particle tracking simulations are common and diverse in their formulation. The reader is recommended to consult the references for more information and options than are presented here<sup>13,14,19</sup>. One of the most common integrators for the equations of motion presented in Eq. (2) and Eq. (3) is the leapfrog method, particularly what is sometimes referred to as the staggered leapfrog method.

Fig. 3 below is a visual depiction of this leapfrog method. The leapfrog method is advantageous to computational simulations for several reasons. First, it requires only one force evaluation per time step. This is more clearly seen in Eq. 4 and Eq. 5 below. Since there are relatively few computations required to advance the simulation by a time-step, the method is highly efficient in terms of computational power required. In addition, the leapfrog method has minimal storage requirements consisting of only one previous position or velocity in time. The error of the leapfrog method for a single time step,  $\Delta t$  converges at  $\Delta t^3$ , and for a full simulation converges as  $\Delta t^2$ . Thus the method is considered a second-order method. This is just one example of time-integration; however, there are numerous other related schemes including the velocity Verlet algorithm which are not discussed.

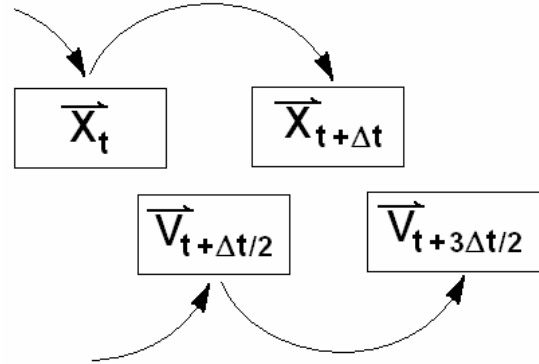


Figure 4. Leapfrog Method Schematic

Applying the staggered leapfrog method as shown in Fig. 4 to the equations of motion gives us the set of equations:

$$\vec{V}_{t+\Delta t/2} = \frac{q\Delta t}{m_e} (\vec{E} + \vec{V} \times \vec{B})_t + \vec{V}_{t-\Delta t/2} \quad (4)$$

$$\vec{x}_{t+\Delta t} = \Delta t \vec{V}_{t+\Delta t/2} + \vec{x}_t \quad (5)$$

where the subscripts (e.g.  $t + \Delta t$ ) denote the time interval each variable is evaluated at, and  $\Delta t$  is the time step. With this formulation, we notice that one problem which will arise is how we shall determine the velocity-dependent force in Eq. 4 stemming from the interaction with the magnetic field. Determining this force requires knowledge of the velocity at a time step for which the velocity is not actually calculated. One way of circumventing this problem is to introduce the following approximation in the force term following Buneman<sup>20</sup>:

$$\vec{V}_t \approx \frac{\vec{V}_{t+\Delta t/2} + \vec{V}_{t-\Delta t/2}}{2} \quad (6)$$

Continuing with the substitution of Eq. 6 into Eq. 4 yields:

$$\vec{V}_{t+\Delta t/2} = \frac{q\Delta t}{m_e} \left( \vec{E}_t + \left( \frac{\vec{V}_{t+\Delta t/2} + \vec{V}_{t-\Delta t/2}}{2} \right) \times \vec{B}_t \right) + \vec{V}_{t-\Delta t/2} \quad (7)$$

Eq. 7 is implicit, but fortunately can be easily solved. Expanding the cross-product term:

$$\vec{V}_{t+\Delta t/2} = \frac{q\Delta t}{m_e} \left( \vec{E}_t + \frac{1}{2} \vec{B}_t \vec{V}_{t+\Delta t/2} + \frac{1}{2} \vec{B}_t \vec{V}_{t-\Delta t/2} \right) + \vec{V}_{t-\Delta t/2} \quad (8)$$

where

$$\vec{B}_t = \begin{bmatrix} 0 & B_z & -B_y \\ -B_z & 0 & B_x \\ B_y & -B_x & 0 \end{bmatrix}_t \quad (9)$$

Rearranging Eq. 8 to group like terms together gives:

$$\left( \vec{I} - \frac{q\Delta t}{2m_e} \vec{B}_t \right) \vec{V}_{t+\Delta t/2} = \frac{q\Delta t}{m_e} \vec{E}_t + \left( \vec{I} + \frac{q\Delta t}{2m_e} \vec{B}_t \right) \vec{V}_{t-\Delta t/2} \quad (10)$$

where the identity matrix is given by:

$$\vec{I} = \begin{bmatrix} 1 & 0 & 0 \\ 0 & 1 & 0 \\ 0 & 0 & 1 \end{bmatrix} \quad (11)$$

Finally, the new velocity is found from:

$$\vec{V}_{t+\Delta t/2} = \left( \vec{I} - \frac{q\Delta t}{2m_e} \vec{B}_t \right)^{-1} \frac{q\Delta t}{m_e} \vec{E}_t + \left( \vec{I} - \frac{q\Delta t}{2m_e} \vec{B}_t \right)^{-1} \left( \vec{I} + \frac{q\Delta t}{2m_e} \vec{B}_t \right) \vec{V}_{t-\Delta t/2} \quad (12)$$

Numerous researchers suggest splitting this equation up into more manageable parts, however, depending on the simulation's demands for computational power, this may not be necessary. One such method separates the electric and magnetic components of the Lorentz force by introducing two new virtual velocities<sup>18</sup>:

$$\vec{V}^a = \vec{V}_{t-\Delta t/2} + \frac{q\Delta t}{2m_e} (\vec{E})_t \quad (13)$$

$$\vec{V}^b = \vec{V}_{t+\Delta t/2} - \frac{q\Delta t}{2m_e} (\vec{E})_t \quad (14)$$

where  $\vec{V}^a$  and  $\vec{V}^b$  are the virtual velocities. Substituting Eq. (13) and Eq. (14) into Eq. (7) leads to the following result:

$$\vec{V}^b = \frac{q\Delta t}{m_e} \left( \frac{\vec{V}^a + \vec{V}^b}{2} \right) \times \vec{B}_t + \vec{V}^a \quad (15)$$

In practice, one first calculates  $\vec{V}^a$  from Eq. (15), then  $\vec{V}^b$  from Eq. (17), and finally the updated velocity from Eq. (9). The method employed in this research utilizes Eq. 12 which will here on be referred to as the Buneman leapfrog method.

In addition to the complication arising from the velocity dependent Lorentz force, initial conditions must be specified at staggered starting times for the staggered leapfrog method to be applied directly. In this sense, the method is not considered to be “self-starting”. Consequently, a “self-starting” method such as the Forward Euler method is sometimes utilized to take the first half-step in velocity as:

$$\vec{V}_{\Delta t/2} = \frac{q\Delta t}{m_e} (\vec{E} + \vec{V} \times \vec{B})_0 + \vec{V}_0 \quad (16)$$

where the subscript “0” is the specified initial condition value of a parameter.

There are many other possible remedies for the velocity-dependent force calculation at an intermediate time-step<sup>13</sup>. One is to reformulate the problem using another method such as a Predictor-Corrector type method<sup>17</sup> or a Runge-Kutta type algorithm. These methods are not discussed here.

As will be shown later, one can obtain reasonable results by applying the leapfrog algorithm directly to Eq. (2) and Eq. (3) in a modified manner as:

$$\vec{V}_{t+\Delta t} = \frac{2q\Delta t}{m_e} (\vec{E} + \vec{V} \times \vec{B})_t + \vec{V}_{t-\Delta t} \quad (17)$$

$$\vec{x}_{t+\Delta t} = 2\Delta t \vec{V}_t + \vec{x}_{t-\Delta t} \quad (18)$$

Some of the centering of the leapfrog algorithm is lost as we are now calculating both velocity and position at each time-step, but we avoid having to perform calculations at time-steps where data is not present. This modified method is explicit in velocity, whereas, the Buneman leapfrog method is implicit. One common downside of an implicit method in this application is that it requires a more complex solution at each time-step. However, a benefit of implicit methods is that they have more favorable stability characteristics<sup>16,19</sup>.

To compare and contrast the accuracy of the staggered leapfrog method with other methods and an analytical solution, the simplified problem of an electron orbiting in a uniform constant magnetic field with a velocity perpendicular to the applied magnetic field is investigated. The analytical solution for such a case is a closed loop with a radius  $r$  defined as:

$$r = \frac{m_e |\vec{V}|}{q |\vec{B}|} \quad (19)$$

Fig. 5, 6, and 7 below show the error comparison. Figure 5 below shows the resultant trajectories of simulated electrons. The initial velocity was taken to be  $10^5$  m/s in the positive x-direction, and the magnetic field strength is 400G. The expected gyration radius is then  $14.2\mu\text{m}$  which is confirmed in Fig 5 below. The trajectories shown represent the 99<sup>th</sup> orbit of the electrons as calculated with a time step of 3% of the orbital period. The 99<sup>th</sup> orbit is taken so sufficient time has elapsed to accumulate a visible error. The black line represents the analytical solution, the red circles are the points calculated with the staggered leapfrog method, and the blue squares are the points calculated with the Adam’s Bashforth method. Not all of the points are shown for clarity. Points calculated with the modified leapfrog method and the forward Euler method are not shown in Fig. 5, but the error trends appear in Fig. 6 and 7. In Fig. 5, close examination reveals that the Buneman leapfrog method is closer to the analytical solution. The Adam’s Bashforth method, though still highly accurate, does not match the analytical solution as well.

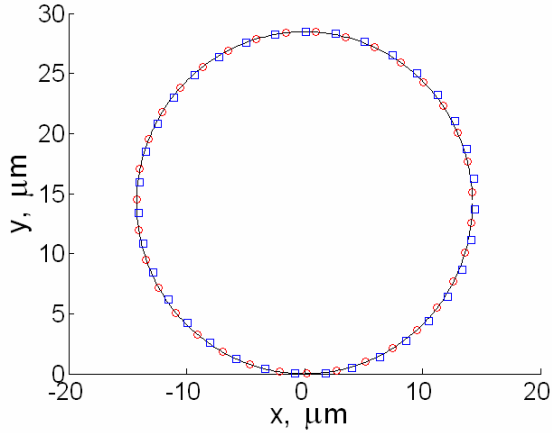


**Figure 5. Electron trajectories computed with Adams Bashforth (squares) and Buneman leapfrog method (circles) compared to analytical solution (solid line).**

error substantially.

Figure 7 shows the error based on a comparison of the numerically calculated gyration radius with the analytical radius. Again, the time-step utilized was 1% of the orbital period. Since the radial error oscillates throughout a cycle, the average error is shown as a linear trend-line in addition to the actual data points. Both the modified leapfrog and Buneman leapfrog methods show minute radial error overall, but considerable oscillations with a magnitude on the order of 2%. It is well known

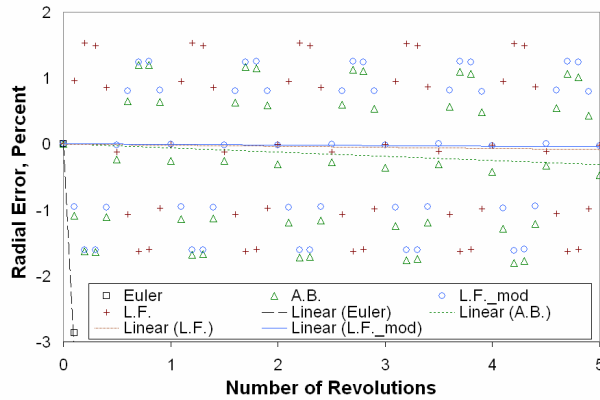


**Figure 7. Radial error comparisons.**

shows a top down view of some representative trajectories for electrons released with velocities with a magnitude distributed about  $3 \times 10^5 \text{ m/s}$  and with random direction from the cathode which is positioned at the location  $x = 0.06\text{m}$ ,  $y = 0.06\text{m}$ , and  $z = 0.02\text{m}$ . The figures show 10 trajectories superimposed and are calculated with a time-step which varies according to the local magnetic field strength as  $\Delta t = 0.01/\omega_{ce}$  (1% of the orbital period). Only every 20<sup>th</sup> point is shown. Figure 8 shows the same simulation results but viewed from the side. The inner and outer limits of the thruster channel are denoted with the bold black lines in the figure.

Figure 6 illustrates the energy-based error evolution with increasing iterations. The data in this figure were calculated using a time step of 1% of the orbital period. The data is plotted versus the number of gyrations of the electron about the magnetic field axis. There are several features to note in this figure. The Buneman leapfrog method, denoted “L.F.” in the figure legend, has the lowest energy-based error which at this point is mostly round-off error. The modified leapfrog method, denoted “L.F.\_mod” in the legend, shows oscillatory error behavior, and the forward Euler method, denoted “F.E.” in the legend, has such high error that it is not a candidate method with this time-step size. Furthermore, since it is a globally first-order method, the time step would have to be significantly reduced to improve the

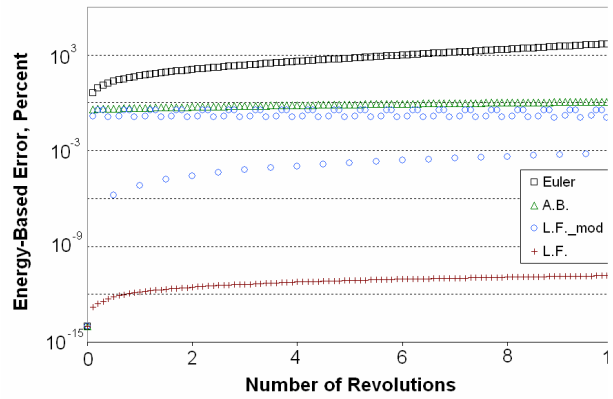


**Figure 6. Energy-based error comparisons for Forward Euler, Adams Bashforth, and leapfrog numerical integration methods.**

that the Buneman leapfrog method, as presented in Eq. 12 has both a phase and radial error which can be remedied if necessary<sup>19</sup>. The Adam’s Bashforth method shows oscillations of the same magnitude, however, from the trend-line it is clear that this error is not remaining centered about zero. The Forward Euler method error is so large that only two points can be seen in Fig. 7.

## IV. Results

The simulation has been run with numerous different integrating methods and time steps. Figure 9 below

Figure 10 and Fig. 11 show the same results but with a cathode at  $x = 0.05\text{m}$ ,  $y = 0.05\text{m}$ , and  $z = 0.02\text{m}$  and with the Buneman leapfrog method as the time-integrator. One additional difference is that only six trajectories are superimposed in Fig. 10 and Fig. 11.

The effect of varying cathode position has so far only been studied with the Adam's Bashforth method and the modified leapfrog method. Figure 12 below illustrates the high sensitivity to cathode position of the Adam's Bashforth method with an oblique view of the resultant trajectories. The electrons in this case are seen to form a tight ring when the cathode is moved to  $x = 0.04\text{m}$ ,  $y = 0.04\text{m}$ ,  $z = 0.02\text{m}$ . Table 1 provides further evidence of this sensitivity for the modified leapfrog method as well. All of the data in Table 1 were obtained with a time step of 1% of the orbital period. The Adam's Bashforth method is abbreviated "AB", and the modified leapfrog method is denoted "LF-mod".

In addition to these trajectories, statistics concerning the electrons' final locations and their motion axially and

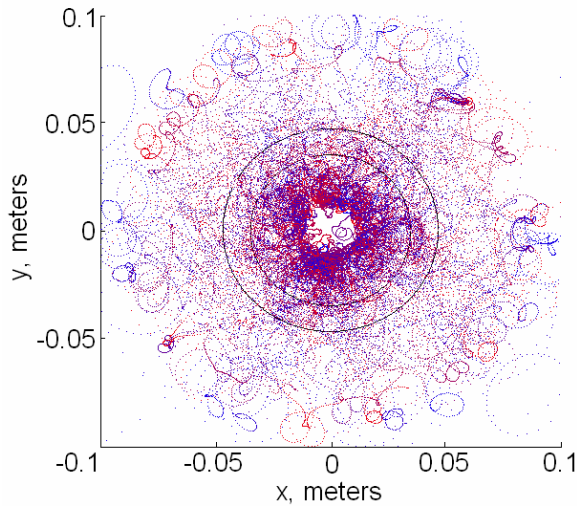


**Figure 9. Electron trajectories calculated with the Adam's Bashforth method.**

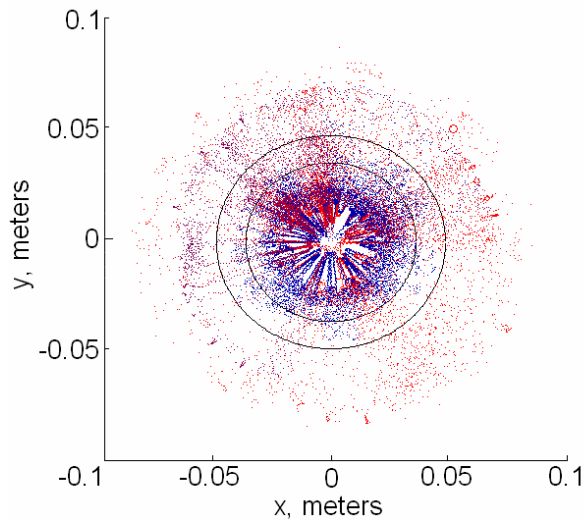


**Figure 11. Electron trajectories calculated with the Buneman leapfrog method.**

azimuthally (with the axis of rotation oriented along  $z$ ) are stored. An average azimuthal distance is currently estimated by assuming an average radius equal to the radius to the center of the channel of the Hall thruster (in this case 41mm). From this information, a coarse

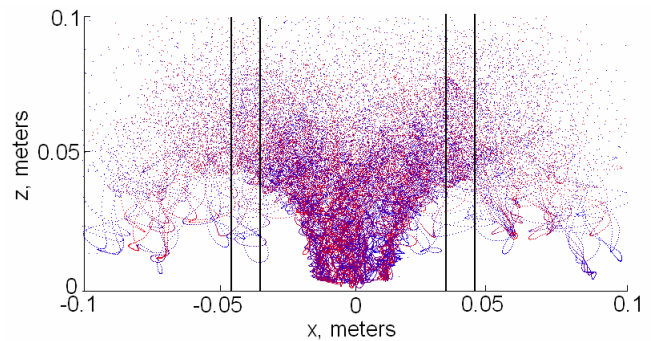


**Figure 8. Electron trajectories calculated with the Adam's Bashforth method.**

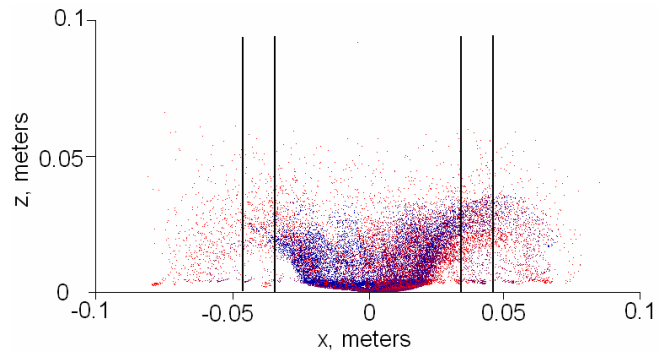


**Figure 10. Electron trajectories calculated with the Buneman leapfrog method.**

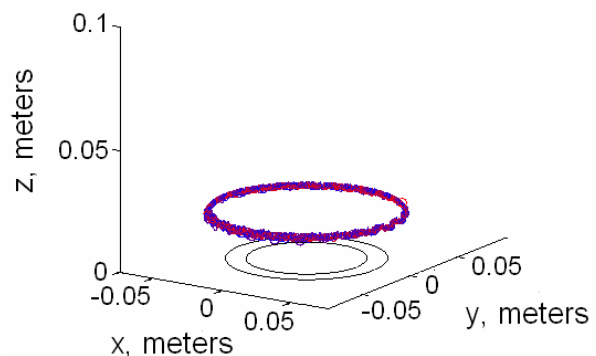


**Figure 12. Electron trajectories calculated with the Adam's Bashforth method with a shifted cathode.**

estimation of the Hall parameter,  $\beta$ , can be obtained as shown in Table 2. All of the information in Table 2 was obtained with a cathode positioned at  $x = 0.05\text{m}$ ,  $y = 0.05\text{m}$ , and  $z = 0.02\text{m}$ . The approximated Hall parameter is simply the ratio of the azimuthal distance traveled to the axial distance traveled considering electrons which end up reaching the channel of the thruster. Also shown in Table 2 is the influence of changing time-step on the current and  $\beta$  statistics. The last row of Table 2 which is italicized represents preliminary data taken for the Buneman leapfrog method. The other five rows represent data obtained with the modified leapfrog method.

Cathode Position (x y z) (m)	Method	Plume Current (%)	Channel Current (%)
0.05 0.05 0.010	AB	100.0	0.0
0.05 0.05 0.015	AB	100.0	0.0
0.05 0.05 0.025	AB	100.0	0.0
0.05 0.05 0.020	LF-mod	84.3	15.0
0.05 0.05 0.025	LF-mod	83.0	14.9
0.06 0.06 0.005	LF-mod	80.8	18.8
0.06 0.06 0.010	LF-mod	80.0	20.0
0.06 0.06 0.015	LF-mod	78.6	21.0
0.06 0.06 0.025	LF-mod	82.7	17.3

**Table 1. Adam’s Bashforth and modified leapfrog method cathode sensitivity.**

$\Delta t * \omega_{ce}$	Plume Current (%)	Channel Current (%)	Average Azimuthal Distance (m)	$\beta$
0.01	91.53	8.24	0.0264	1.32
0.005	80.00	15.00	0.0183	0.91
0.001	67.86	26.43	0.0318	1.59
0.0005	81.02	13.87	0.0402	2.01
0.0001	75.71	14.29	0.0860	4.30
<i>0.01</i>	<i>88.80</i>	<i>9.90</i>	<i>0.0442</i>	<i>2.21</i>

**Table 2. Electron current statistics for calculations made with the leapfrog methods.**

## V. Discussion

Results of a 3D discrete electron transport model of the near field of a Stanford Hall thruster have been presented. Preliminary results are encouraging, particularly those involving the Buneman leapfrog method which has only been studied to a limited extent at this point in time. As shown in Table 1, with the model utilized currently, which does not include the effect of instabilities or collisions in the near field, the Adam’s Bashforth method shows no electron current reaches the anode, whereas the modified leapfrog method shows a relatively high electron current to the anode. The single entry pertaining to the Buneman leapfrog method in Table 2 suggests a current similar to the modified leapfrog method. However, the Buneman leapfrog method and the Adam’s Bashforth method are similar in their distribution of electron trajectories as evidenced by Fig. 8 through Fig. 11. Further work is required to validate one method or the other.

With refinement of the estimated electric potential utilized, the results will provide insight into several features of Hall thrusters which are currently understood to a limited extent. Such features include the bright central beam visible in the near field as well as the driving mechanism for the anode/plume current ratios measured experimentally. In addition, this type of model may suggest regions of optimal cathode placement based on desired electron current characteristics.

Future work includes experimentally measuring the electric potential in the near-field on a large number of points to utilize in the model as well as using the model to produce qualitative electron density maps in the near field

which can readily be compared with experimental results. In addition, a spatial map of the electron energy distribution function is being generated. Finally, the effects of collisions and instabilities, which were neglected in these results, will be examined and implemented.

### Acknowledgments

A. W. Smith thanks the National Defense Science and Engineering Graduate Fellowship program for its financial support as well as the Air Force Office of Scientific Research, and Nicolas Gascon, Ph.D. for his tireless patience and advice.

### References

- <sup>1</sup>Fife, J.M., "Hybrid-PIC Modeling and Electrostatic Probe Survey of Hall Thrusters," Ph.D. Dissertation, Aeronautics and Astronautics Dept., Massachusetts Institute of Technology, Cambridge, MA, 1998.
- <sup>2</sup>Smirnov, A., Raitses, Y., and Fisch, N. J., "Plasma Measurements in a 100W Cylindrical Hall Thruster," *Journal of Applied Physics*, Vol. 95, Num. 5, 2004, pp. 2283-2292.
- <sup>3</sup>King, L.B., "Transport Property and Mass Spectral Measurements in the Plasma Exhaust Plume of a Hall-effect Space Propulsion System," Ph.D. Dissertation, Department of Aerospace Engineering, University of Michigan, Ann Arbor, MI, 1998.
- <sup>4</sup>Staack, D., Raitses, Y., and Fisch, N.J., "Temperature Gradient in Hall Thrusters," Princeton Plasma Physics Laboratory, PPPL-3905, Princeton University, Princeton, NJ, 2003.
- <sup>5</sup>Hofer, R. H., and Gallimore, A. D., "Recent Results From Internal and Very-Near-Field Plasmas Diagnostics of a High Specific Impulse Hall Thruster", NASA/CR – 2003-212604, IEPC-2003-037, 2003.
- <sup>6</sup>Raitses, Y., Keidar, M., Staack, D., and Fisch, N. J., "Effects of Segmented Electrode in Hall Current Plasma Thrusters," *Journal of Applied Physics*, Vol. 92, Num. 9, 2002, pp 4906-4911
- <sup>7</sup>Linnell, J. A., and Alec D. Gallimore, "Internal Plasma Structure Measurements of a Hall Thruster Using Plasma Lens Focusing," AIAA/ASME/SAE/ASEE Joint Propulsion Conference, AIAA-2005-4402, 2005.
- <sup>8</sup>Beal, B. E., Gallimore, A. D., and Hargus, W. A., Jr., "The Effects of Cathode Configuration on Hall Thruster Cluster Plume Properties," AIAA-2005-3678, 2005.
- <sup>9</sup>Garrigues, L., Bareilles, J., Boeuf, J.P., and Boyd, I.D., "Modeling of the Plasma Jet of Stationary Plasma Thruster," *Journal of Applied Physics*, Vol. 91, Num. 12, 2002, pp. 9521-9528.
- <sup>10</sup>Tacconga, F., Longo, S., Capitelli, M., and Schneider, R. "Stationary Plasma Thruster Simulation," *Computer Physics Communications*, Num. 164, 2004, pp. 160-170.
- <sup>11</sup>Tacconga, F., Longo, S., Capitelli, M., "Very-Near-Field Plume Simulation of a Stationary Plasma Thruster," *Applied Physics proofs*, 2004.
- <sup>12</sup>Tacconga, F., Longo, S., Capitelli, M., "Very-Near-Field Plume Simulation of a Hall Thruster".
- <sup>13</sup>Hargus, W. A., Jr., "Investigation of the Plasma Acceleration Mechanism within a Coaxial Hall Thruster," Ph.D. Dissertation, Department of Mechanical Engineering, Stanford University, Stanford, CA, 2001.
- <sup>14</sup>FEMM, Finite Element Method Magnetics, Software Package, Version 4.0, David Meeker, 2004.
- <sup>15</sup>Birdsall, C.K., and Langdon, A.B. "Plasma Physics Via Computer Simulation," Institute of Physics Publishing, Bristol and Philadelphia, 1991.
- <sup>16</sup>Moin, P., "Fundamentals of Engineering Numerical Analysis," Cambridge University Press, 2001.
- <sup>17</sup>Lundstrom, J., "Langevin Dynamics in Magnetic Disorder," Masters Thesis, Dept. of Applied Physics and Mechanical Engineering, Lulea University of Technology, Lulea, Sweden, 2002.
- <sup>18</sup>Boris, J.P., "Relativistic Plasma Simulation Optimization of a Hybrid Code," *Proceedings of the Fourth Conference on Numerical Simulation of Plasmas*, 3-67, Naval Res. Lab, Washington, D.C. 1970
- <sup>19</sup>Hockney, R.W., and Eastwood, J.W. "Computer Simulation Using Particles," Taylor & Francis Group Publishing, New York, New York, 1988.
- <sup>20</sup>Buneman, O., "Time Reversible Difference Procedures," *Journal of Computational Physics*, Vol. 1, 1967, pp. 517-535.